Effect of Oxygen Partial Pressure and Temperature on the Oxidation Behavior of SiB_6

MUHAMMAD A. IMAM , JACOB S. YOUNG, and RAMANA G. REDDY

The oxidation kinetics of silicon hexaboride (SiB_6) was studied at different partial pressures of oxygen. The specific weight gain was measured at 1173 K, 1223 K, and 1273 K for $P_{O_2} = 0.1$, 0.23, and 0.33 atm using thermogravimetric analysis. The conventional empirical expressions for oxidation were observed at all selected oxygen partial pressures and temperatures. The structural characterization of the oxidation product was characterized using XRD and FT-IR, with SiB_6, SiO_2, B, and amorphous B_2O_3 observed after oxidation for 25 hours. The oxidation surface morphology was also characterized to obtain the oxidation product size, ranging from 4.54 to 24.69 μm with increasing P_{O_2} and temperature. The diffusional activation energy for the oxidation process was also calculated from the empirical constant, obtained from the mathematical fitting of the specific weight gain with time. The oxidation activation energies for SiB_6 are 250.72, 235.64, and 232.65 kJ/mol at $P_{O_2} = 0.1$, 0.23, and 0.33 atm, respectively.

https://doi.org/10.1007/s11663-019-01749-z
© The Minerals, Metals & Materials Society and ASM International 2019

I. INTRODUCTION

WITHIN the Si-B system, boron-rich compositions have drawn recent attention due to their high-temperature performance as thermoelectric (TE) materials and thermal barrier coatings (TBC).[1] The thermodynamic properties and phase diagram of the Si-B system, as well as other boride systems, have been thoroughly studied previously.[2–14] Experimental data indicate the presence of various binary phases, namely SiB_3, SiB_6, and SiB_n ($n = 14$ to 50).[15] Among these phases, SiB_6 is the most thermodynamically stable in an inert atmosphere.[3,6,7,11] As a result, SiB_6 is one of the prominent thermal emittance agents used for protective ceramic coatings of space vehicles and combustion chambers to re-radiate thermal energy.[16,17] Oxidation of silicon borides is known to reduce critical thermoelectric and transport properties.[18] The effect of partial pressure of oxygen and temperature on the oxidation kinetics of Si-B materials is an essential factor toward better optimization of TE and TBC performance.

Boron and silicon oxidation has been well studied in the literature.[19–24] Pure boron particles generally react readily with oxygen, forming a thick, vitreous, molten layer of B_2O_3 on the surface, as boron oxide melts at a low temperature (~ 723 K) and has a wide liquidus range before boiling at 2340 K.[25] The literature suggests that oxidation of B is very slow and leads to only partial oxidation of B due to scale formation of B_2O_3.[26] The oxidation behavior of Si is dependent upon the formation of a uniform, amorphous, thin layer of SiO_2, inhibiting oxygen diffusion through it as the layer grows in thickness. This limitation of oxygen diffusion heavily influences the crystallization process of SiO_2.[27–29]

Due to the complexity of the oxidation processes involved with intermetallic Si-B materials, the oxidation kinetics of SiB_6 is still not completely understood. Different studies suggest that high-temperature oxidation related to intermetallics involves complex oxidation kinetics of multiple phases.[30–32] In the Si-B system, limited oxidation studies were found in the literature, referring to the oxidation resistance at elevated temperatures.[18] No oxidation mechanism has been presented due to the complex nature of the process. A non-isothermal oxidation study of SiB_6 in air from 873 K to 1473 K for 25 hours found that SiO_2 and B_2O_3 formed during the oxidation process, but a detailed mechanism of the simultaneous oxide formation was not reported.[18] A similar study of SiB_3 in air from 473 K to 1273 K detailed the oxidation resistance, experimental specific weight gain (90 pct), and theoretical oxide formation (190 pct), but the oxidation kinetics and detailed mechanism were not reported.[10] The difference between experimental and theoretical weight gain was attributed to the effect of oxygen partial pressure.

The oxidation reaction involving SiB_6 can be summarized with Eq. [1][18,33]:

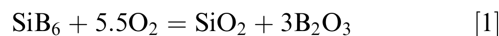

$$SiB_6 + 5.5O_2 = SiO_2 + 3B_2O_3 \qquad [1]$$

MUHAMMAD A. IMAM, JACOB S. YOUNG, and RAMANA G. REDDY are with the Metallurgical and Materials Engineering, The University of Alabama, Tuscaloosa, AL 35487. Contact e-mail: rreddy@eng.ua.edu

Article published online December 9, 2019.

$$\Delta G = -RT \ln \frac{1}{(P_{O_2})^{5.5}}. \quad [2]$$

Equation [2] describes the oxygen partial pressure dependency for the SiB_6 oxidation thermodynamic favorability, where ΔG is the change in Gibbs energy. The activities of SiB_6, SiO_2, and B_2O_3 are assumed to be 1 in the equilibrium constant term $\ln(K)$, as they are condensed solids. A detailed thermodynamic calculation was performed using HSC 7.1 (Figure 1) to understand the oxidation behavior of SiB_6 under different conditions. In Figure 1, equilibrium composition calculations of SiB_6 + O_2(g) initial condition at 1273 K were completed over a range of O_2 content. As seen in Figure 1, Si is preferentially oxidized over B at low oxygen contents. The amount of B_2O_3 formed is nonzero at low O_2 content, but negligible compared to SiO_2 formation. Boron is also preferentially formed at low amounts of O_2, with a peak and decrease as oxygen content increases.

In this study, the simultaneous oxidation kinetics of SiO_2 and B_2O_3 from SiB_6 was established by varying the oxygen partial pressure from 0.1 to 0.33 atm. The standard TGA weight gain method was used to obtain the isothermal oxidation at different temperatures for 25 hours. The mathematical fitting of the specific weight gain with time was used to understand the partial pressure dependency of the simultaneous oxidation mechanism.

II. EXPERIMENTAL PROCEDURE

A. *Materials and Method*

Silicon hexaboride was prepared from 99.95 pct Si (Alfa Aesar) and 99.99 pct B (Alfa Aesar) powders. The Si and B were mixed in stoichiometric quantities within an argon atmosphere glove box, transferred into a sealed jar, and jar-milled for 24 hours to obtain a homogeneous mixture of silicon and boron. After that, 13-mm-diameter pellets were made from the homogeneous mixture using a Carver cold pressing unit at a pressure of 5000 psi for 5 minutes. The pellets were then melted in an arc melter (ABJ338, Materials Research Furnaces Inc.). A 200-ampere operating current was used to form the arc in an ultra-high-pure argon atmosphere. Ti getter was used to protect the sample surface from oxidation. This process was done 4 times, flipping between melts, to ensure homogeneity. Each melted ingot was wrapped with Ta foil and transferred into a vacuum-sealed quartz ampoule for annealing. The annealing was done in an MTI (GSL-1100X) quartz tube furnace at 1273 K for 24 hours to reach the equilibrium composition. In Figure 2, step-by-step preparation of SiB_6 is shown schematically.

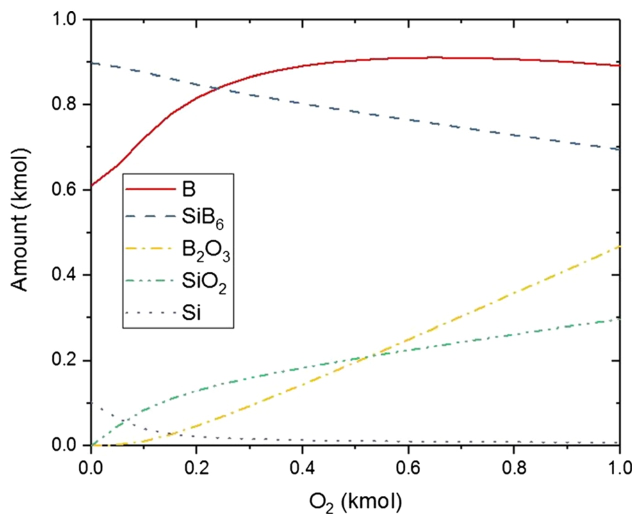

Fig. 1—Equilibrium composition diagram of SiB_6, SiO_2, and B_2O_3 at 1273 K with change of oxygen content from HSC software.[34]

B. *Characterization*

The weight gain data were measured using a Labsys thermogravimetric analyzer (TGA). Isothermal TGA was performed at three temperatures (1173 K, 1223 K, and 1273 K) while maintaining a range of oxygen partial pressures (P_{O_2} = 0.1, 0.23, and 0.33 atm) for 25 hours. Ultra-high-pure Ar gas was used as a protecting gas during the heating, cooling, and isothermal holding periods. X-ray diffraction of the oxidation product was carried out using the Philips MPD X'Pert after the TGA experiment to confirm the crystalline phases after oxidation. The XRD operating conditions were 45 kV and 40 mA, 0.001 deg per sec scan rate from 5 to 80 deg Bragg's angle (2θ). The Cu Kα target was used to produce the incident X-ray beams of 1.54 Å. Further chemical structural characterization of the oxidation product was performed using Fourier-transform infrared spectroscopy (FTIR), carried out on a PerkinElmer Universal ATR instrument in the range of 650 to 4000 cm^{-1}. For the morphological and elemental characterization, FESEM and EDS were performed on FESEM model JEOL JSM 7000F equipped with Oxford EDS detector.

III. RESULTS AND DISCUSSION

A. *Effect of Partial Pressure of Oxygen (P_{O_2}) and Temperature*

The specific weight gain of the SiB_6 samples after 25 hours as a function of temperature and oxygen partial pressure was obtained using TGA. As seen from Figures 3(a) through (c), specific weight gain increases with higher temperatures and higher oxygen partial pressures. Two-step parabolic oxidation behavior was observed for the selected partial pressures of oxygen (Figures 3(a) through (c)). As seen from Figure 3, two linear portions (dotted lines) are identified which indicates the two-step oxidation process of SiB_6. The empirical reaction rate constant, k_p, was calculated from the relationship between the weight gain per unit area, $\Delta w/a$, and time, $t^{1/2}$,[35] shown in Eq. [3]:

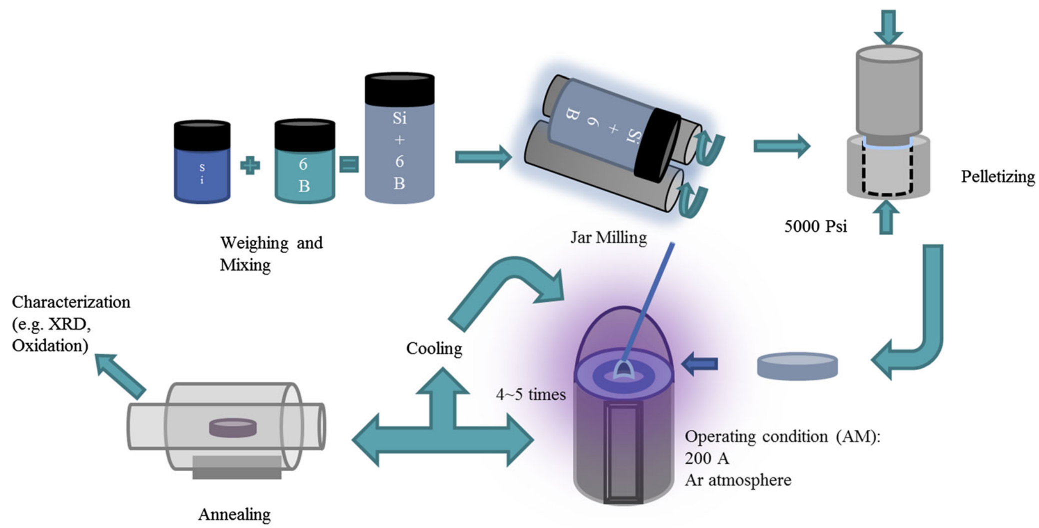

Fig. 2—Schematic of the preparation of the SiB_6 intermetallic (step by step—jar milling, pelletizing, arc melting, and annealing).

Fig. 3—Oxidation behavior (specific weight gain *vs* $t^{1/2}$) of SiB_6 at 1173 K, 1223 K, and 1273 K exposed to (*a*) P_{O_2} = 0.33 atm, (*b*) P_{O_2} = 0.23 atm, and (*c*) P_{O_2} = 0.1 atm (dotted lines indicate the linear portions).

$$\left(\frac{\Delta w}{a}\right)^2 = k_p t. \quad [3]$$

B. *Characterization of Oxide Formation*

X-ray diffraction (XRD) analysis was performed to characterize the phase structure after the oxidation process, shown in Figure 4. Crystalline phases of SiO_2, SiB_6, and B were identified and matched with their corresponding powder diffraction files: PDF#14-0654, PDF#47-1006, and PDF#31-0207, respectively.

The XRD analysis confirmed the formation of crystalline SiO_2 as a result of oxidation, as well as the existence of unreacted SiB_6 and the formation of B. The oxidation process of Si is initially quick, resulting in the formation of a thin, amorphous $SiO_2 + B$ composite layer, which hinders further diffusion of oxygen to the unreacted SiB_6. As oxygen diffusion slows, crystalline SiO_2 is preferentially formed due to longer reaction time and higher stability than the amorphous structure, similar to the oxidation behavior of pure Si.[27–29] FTIR analysis was also carried out to understand the chemical structure of the oxidized sample. In Figure 5, FTIR analyses of SiB_6, before and after oxidation, are presented. After oxidation, the FTIR spectra have dramatically changed due to change in the chemical structure. Symmetric and asymmetric vibrations of Si-O-Si and B-O were observed at approximately 1075, 796, 1437, and 1185 cm^{-1}, confirming the oxidation of the Si and B from SiB_6. A broad peak around 3200 cm^{-1} represents the symmetric vibration from B-OH, due to the atmospheric moisture absorbed by boron oxide. Although no crystalline boron oxide peak was found from the XRD (Figure 4), the symmetric and asymmetric B-O peaks from FTIR confirmed the formation of amorphous boron oxide. Boron particles form a thick, vitreous layer of B_2O_3 on the parent surface since boron oxide melts at a low temperature (723 K), and it has a wide molten range before boiling at 2130 K,[25] in which the experimental temperature range is within. The formation of amorphous boron oxide was also observed during oxidation of other boride systems, *i.e.*, HfB_2 and HfB_2-SiC.[30,36]

According to thermodynamic equilibrium calculations shown in Figure 1, the formation of SiO_2 is more favorable than boron oxide in the presence of lower O_2 concentration. This phenomenon was further confirmed by the structural characterization using XRD. The formation of boron oxide is delayed due to the two-step oxidation process of SiB_6, *i.e.*, the initial production of SiO_2 and formation of pure B, which then reacts with oxygen (Eq. [1]), which is also confirmed by the slope change of the weight gain *vs* $t^{1/2}$ plot from Figure 3. Hence, the boron oxide does not fully complete formation within this experimental oxidation time:

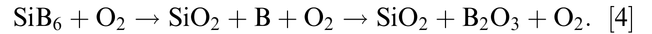

$$SiB_6 + O_2 \rightarrow SiO_2 + B + O_2 \rightarrow SiO_2 + B_2O_3 + O_2. \quad [4]$$

In Figure 6, SEM micrographs of SiB_6 oxidation with varying temperature and oxygen partial pressure are presented. At oxygen partial pressures of $0.1 \le P_{O_2} \le 0.33$ at a given temperature, the oxidation product morphology is similar. The oxidation product sizes measured using ImageJ software from the petal sides are summarized in Table I. With increasing temperature, the flower petal-like oxidation products show a statistically significant increase in size using ANOVA analysis ($p < 0.05$). Although the product size average also increased with increasing oxygen partial pressure, the differences were not found to be statistically significant. This phenomenon further confirmed the temperature dependence of the SiB_6 oxidation behavior shown in Figure 3. Therefore, while oxidation mechanism of SiB_6 does not change over the selected temperature and pressure range, the rate of oxidation increases with temperature.

In Figure 7, the EDS analysis further confirmed the elemental composition of oxide petals comprising of all the products, including Si, O, and B (Figure 7(a)). A line scan of the cross section is shown in Figure 7(b), which confirms the formation of the oxidation layer, in addition to a relatively unoxidized core and an

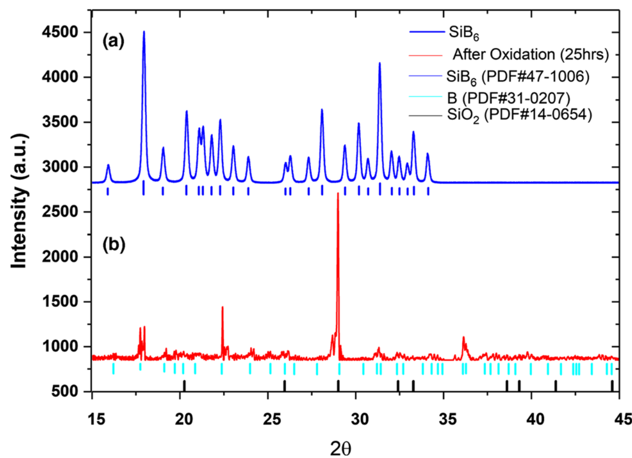

Fig. 4—X-ray diffraction of SiB_6 (*a*) before and (*b*) after oxidation.

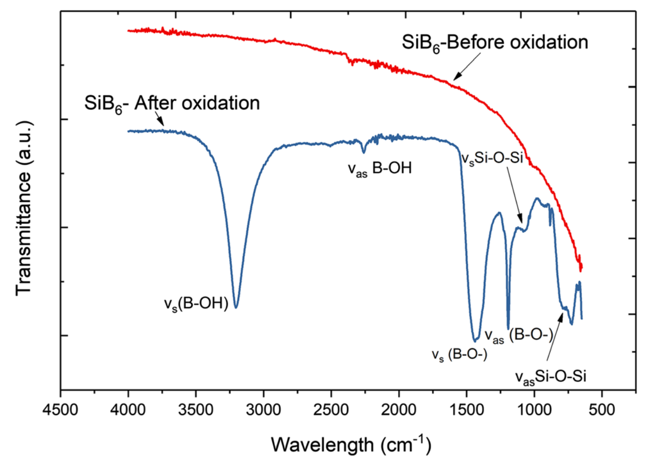

Fig. 5—FTIR spectra of SiB_6 before and after oxidation.

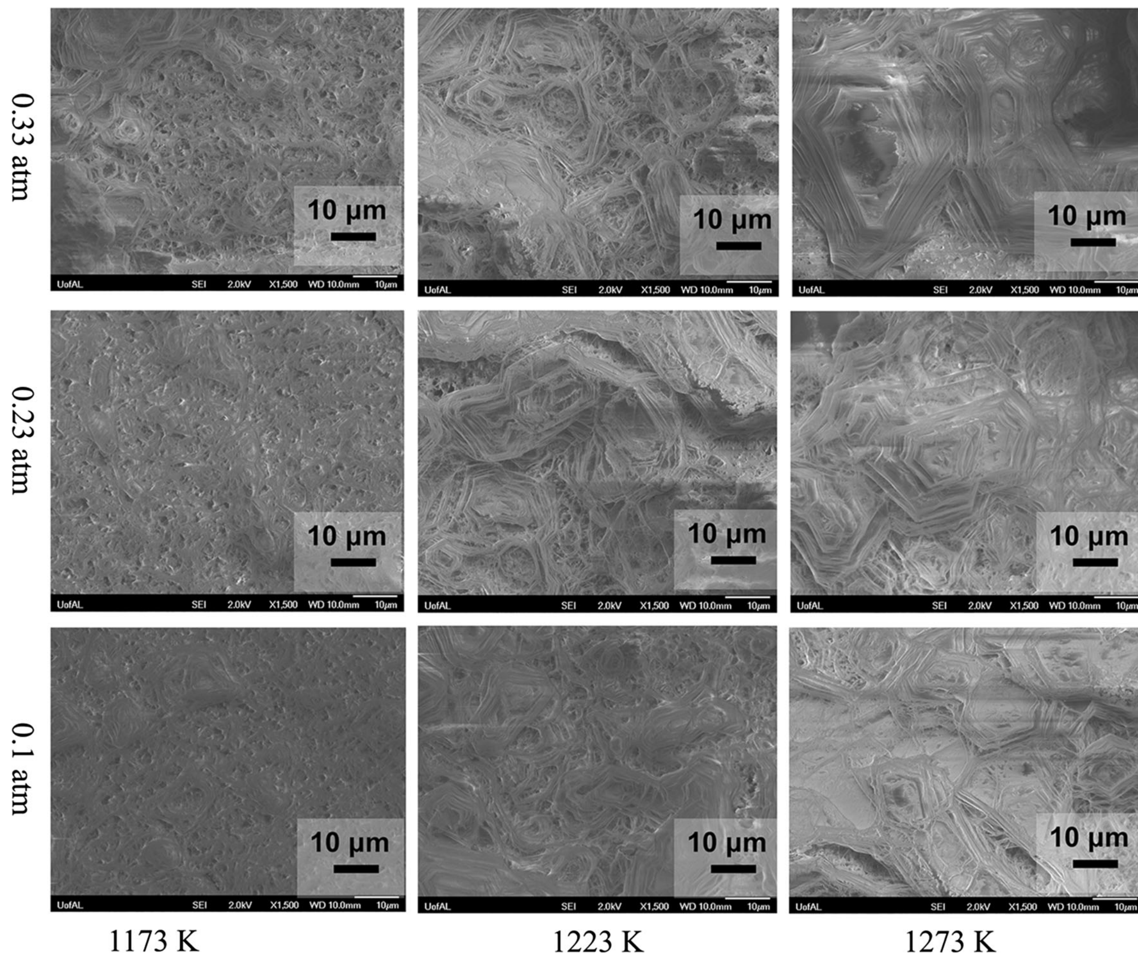

Fig. 6—SEM micrograph of oxidation of SiB_6 at different temperatures and partial pressures of oxygen.

Table I. The Oxidation Product Petal Size at Selected Partial Pressures of Oxygen

P_{O_2} ↓	Oxidation Product Size (μm)		
	T (K)		
	1173	1223	1273
0.1	4.54 ± 4.25	10.53 ± 6.55	19.22 ± 5.75
0.23	4.81 ± 2.04	14.74 ± 3.83	20.23 ± 7.67
0.33	5.38 ± 1.64	15.92 ± 4.36	24.69 ± 8.66

intermediate oxide core layer. The EDS analysis of the oxide and core interface layer is shown in Figure 7(c), where oxygen concentration is lower than the surface oxidation layer. In Figure 7(d), the EDS of the core is shown, where the oxygen concentration is much smaller than the other two layers, which further confirms that oxygen diffusion is lowered by the formation of oxide layers. This phenomenon eventually agreed with the previous literature.[27–29] It needs to be mentioned that the sample was mounted using epoxy resin to observe the cross section, which caused the presence of a C peak in the EDS analysis.

C. *SiB_6 Oxidation Kinetics*

In Figure 8, the variation of the parabolic, empirical rate constant with temperature and partial pressure of oxygen was illustrated from a semi-log plot (Arrhenius type) of the empirical constant, ln k_p *vs* T^{-1} plot. The parabolic nature of oxidation weight gain confirms that the process is diffusion controlled.[25] There is a significant increase in the magnitude of empirical k_p as oxidation temperature and P_{O_2} increase.

The apparent activation energy for diffusion and overall oxidation of SiB_6, determined from the slope of the linear fit of ln k_p *vs* $10^4/RT$, decreases with an increasing partial pressure of oxygen. Linear regression testing yields R^2 = 0.933, 0.944, and 0.932 and p = 0.117, 0.107, and 0.118 for P_{O_2} = 0.33, 0.23, and 0.1, respectively. Therefore, linearity can be observed with approximately 90 pct certainty, with the majority of the unexplainable error likely due to some variability of the P_{O_2} measurement during the high-temperature experimental procedure. The precise measurements of the partial pressure at a high temperature are currently a challenge, but could reduce the uncertainty of future experimental oxidation process. Regression testing between P_{O_2} and E_a yields R^2 = 0.916 and p = 0.187,

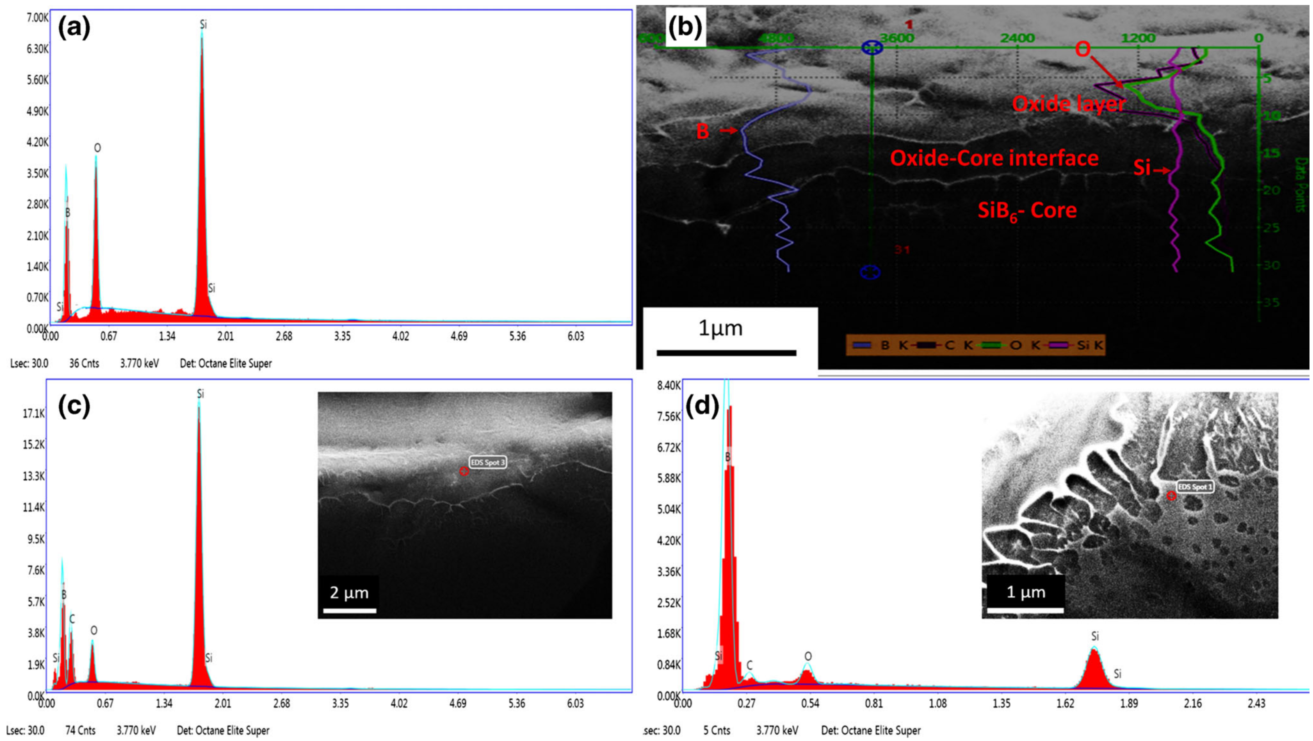

Fig. 7—EDS of (*a*) oxidation petal shown in Fig. 6, (*b*) line scan of oxidation cross section, (*c*) oxide core interface and (*d*) core.

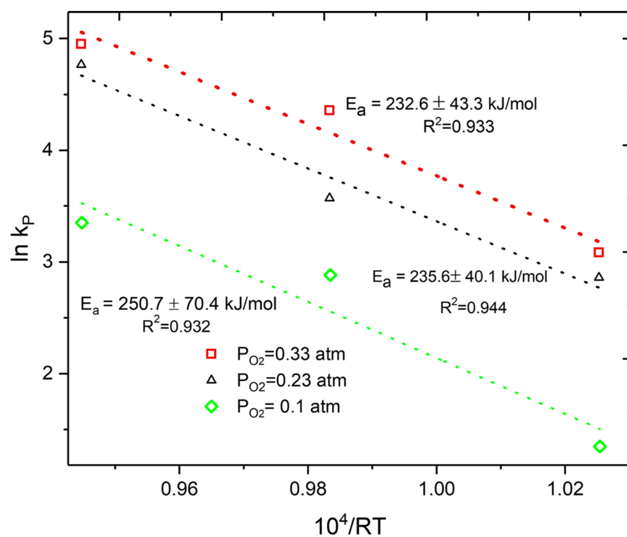

Fig. 8—A semi-log (Arrhenius) plot of ln k_p *vs* T^{-1} for different partial pressures of oxygen.

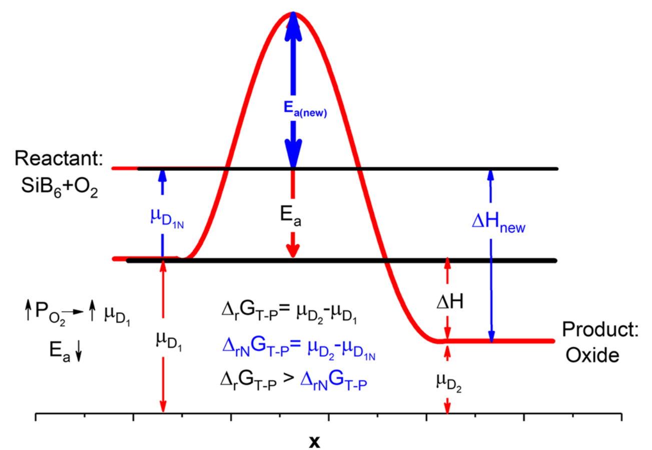

Fig. 9—Effect of P_{O_2} on diffusional activation energy.

proposing that the two variables are greatly related to one another, although they likely have a nonlinear behavior.

This phenomenon agrees with fundamental diffusion theory [37] explained in Figure 9. At an initial condition (given *P* and *T*), there exists an oxygen concentration difference, and therefore a chemical potential (μ) gradient, between the atmosphere and the SiB_6 sample. The chemical potential for oxygen diffusion toward the interface is influenced by the partial pressure of oxygen (P_{O_2}) in the surrounding atmosphere. Molecules tend to move from areas of high concentration to low concentration until equilibrium is reached. The change in Gibbs energy of oxidation (Eq. [1]) depends on the change of the chemical potential of the reactants ($\mu_{D_1}/\mu_{D_{1N}}$) and products (μ_{D_2}), where

$$\Delta G = \sum_{i=1}^{n} \mu_i \mathrm{d}N_i \qquad [5]$$

and

$$\Delta G = \Delta H - T\Delta S. \qquad [6]$$

At a given partial pressure of oxygen, SiB_6 will oxidize assuming a particular activation energy (E_a) is provided, as ΔG is negative (favorable reaction). As oxygen content increases, the concentration difference and reactant chemical potential, μ_{D_1}, increase to μ_{D_2}. As ΔG and ΔH become more negative as a consequence of increased P_{O_2}, E_a becomes smaller. It should be noted that the experimental E_a from this study should be classified as empirical and represents the overall oxidation process of SiB_6, as Si and B oxidize through different reactions with their own E_a.

The oxidation activation energy for SiB_6 calculated from this study is summarized in Table II, along with available literature data for powdered SiB_6, pure Si and B, and similar boride systems. Bulk SiB_6 data are not currently published. As seen from Table II, the bulk SiB_6 has higher activation energy than the compared powdered SiB_6 literature data, which is attributed to a significantly lower surface (reaction) area for bulk samples. Similar phenomena, *i.e.*, surface area effect on the activation energy, was observed in the literature for the pure boron,[38] which is also reported in Table II. In the case of pure boron powder, when the surface area was reduced due to bigger particle size (from 25 to 65 μm), the activation energy increased at a particular partial pressure of oxygen. After comparing our reported activation energies with the literature data, the powder surface area plays a critical role in determining the rate of oxidation. Hence, the difference in surface area is the rate-limiting step for the oxidation of borides. The activation energies for other borides are also reported here to compare with our study to understand the similar borides oxidation. The activation energy for LaB_6 was reported 195 kJ/mol by Chung *et al.*[39] in dry air, which is comparable with our reported data for SiB_6.

In Figure 10, the empirical constant is presented with variations of the partial pressure of oxygen and temperature. Empirical constant increases linearly as the partial pressure of oxygen increases. Higher temperature also increases the empirical constant. The relationship between the empirical constant and the partial pressure of oxygen for SiB_6 oxidation can be explained by the following linear equations:

$$\log k_{1273} = (2.9 \pm 0.2) + (1.4 \pm 0.2) \log P_{O_2} \quad (R^2 = 0.96) \qquad [7]$$

$$\log k_{1223} = (2.4 \pm 0.2) + (1.2 \pm 0.3) \log P_{O_2} \quad (R^2 = 0.93) \qquad [8]$$

$$\log k_{1173} = (2.1 \pm 0.2) + (1.5 \pm 0.3) \log P_{O_2} \quad (R^2 = 0.96). \qquad [9]$$

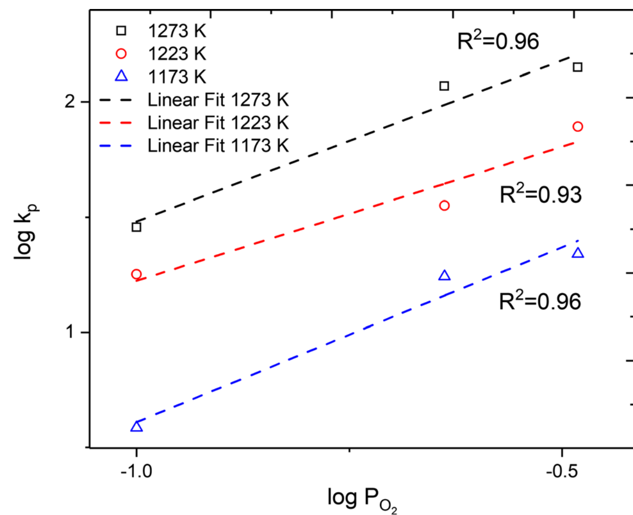

Fig. 10—Variation of the empirical constant with the partial pressure of the oxygen at different temperatures.

Table II. Summarized Oxidation Activation Energy for SiB_6, Si, and B

	Oxidation Activation Energy (kJ/mol)				
	P_{O_2} (Atm)				
Phases	0.1	0.23	0.33	1	Ref.
SiB_6 ($1173 \leq T \leq 1273$ K)	250.72	235.64	232.65		This study
SiB_6 Powder ($873 \leq T \leq 1248$ K)		31.42			Matsushita *et al* [18]
Pure Si ($1100 \leq T \leq 1600$ K)				90.71	Kingery *et al.*[40]
Pure Si ($1073 \leq T \leq 1373$ K)		118.67 (dry air)			Jaegar[41]
Pure B Powder (α) ($790 \leq T \leq 1028$ K)		277.1			Yu *et al.*[42]
Pure B (β) Powder ($790 \leq T \leq 1028$ K)		336.2			Yu *et al.*[42]
Pure B Powder (25 μm)				~184	Yang *et al.*[38]
Pure B Powder (65 μm)				~190	Yang *et al.*[38]
Pure B (α) Sintered ($790 \leq T \leq 1028$ K)				40.6	Yu *et al.*[42]
Pure B (β) Sintered ($790 \leq T \leq 1028$ K)				27.8	Yu *et al.*[42]
HfB_2-SiC ($1623 \leq T \leq 1773$ K)			443.08		Hinze *et al.*[43]
ZrB_2 ($1073 \leq T \leq 1273$ K)				104.5	Trip *et al.*[44]
HfB_2 ($1473 \leq T \leq 1833$ K)				196.5	Berkowitz *et al.*[45]
LaB_6 ($1073 \leq T \leq 1218$ K)		195 (air)		200	Chung *et al.*[39]

Table III. The Empirical Constant of SiB_6 Oxidation

	log k_p		
log P_{O_2}	1273 K	1223 K	1173 K
− 0.48	2.15	1.89	1.34
− 0.64	2.07	1.55	1.24
− 1.00	1.46	1.25	0.59

All of the empirical constants are also summarized in Table III.

IV. CONCLUSION

The oxidation of SiB_6 was studied at elevated temperature (1173 K, 1223 K, and 1273 K) using different oxygen partial pressures (P_{O_2} = 0.1, 0.23, and 0.33 atm). Based on weight gain measurements using TGA, the oxidation rate followed a purely parabolic relationship with time. The structural characterization of the oxidation product was characterized using XRD and FTIR. After oxidation, the primary phases present are SiB_6, SiO_2, B, and amorphous B_2O_3. The oxidation product size was also calculated using SEM from the oxidation surface morphology, where size ranged from 4.54 to 24.69 μm with increasing P_{O_2} and temperature. The activation energy for oxidation diffusion was also calculated from the empirical constant, obtained from a mathematical fitting of the parabolic sections of specific weight gain with time. The oxidation activation energies for SiB_6 are 250.72, 235.64, and 232.65 kJ/mol at P_{O_2} = 0.1, 0.23, and 0.33 atm, respectively. The observed activation energies were compared with the available literature data, following similar trends and magnitude in regard to sample surface area, applied temperature, and oxygen content.

ACKNOWLEDGMENTS

The authors gratefully acknowledge the financial support, Grant No. DMR-1310072, of the National Science Foundation (NSF). The authors would also like to acknowledge the financial support from American Cast Iron Pipe Company (ACIPCO) and Department of Metallurgical and Materials Engineering at the University of Alabama.

REFERENCES

1. B. Armas, C. Combescure, J.M. Dusseau, T.P. Lepetre, J.L. Robert, and B. Pistoulet: *J. Less Common Met.*, 1976, vol. 47, pp. 135–40.
2. Y.O. Esin, S.P. Kolesnikov, B.M. Baev, and A.F. Ermakov: *J. Struct. Prop. Metall. Slag Melts*, 1978, vol. 3, pp. 182–83.
3. A.I. Zaitsev and A.A. Kodentsov: *J. Phase Equilib.*, 2001, vol. 22, pp. 126–35.
4. A.K. Biletskii, A.A. Scheretskii, V.T. Vitusevich, and V.T. Shumihin: *Metals*, 1988, vol. 3, pp. 66–68.
5. R. Noguchi, K. Suzuki, F. Tsukihashi, and N. Sano: *Metall. Mater. Trans. B*, 1994, vol. 25B, pp. 903–07.
6. J. Wu, W. Ma, D. Tang, B. Jia, B. Yang, D. Liu, and Y. Dai: *Procedia Eng.*, 2012, vol. 31, pp. 297–301.
7. B. Armas, C. Combescure, G. Male, and M. Morales: *J. Less Common Met.*, 1979, vol. 67, pp. 449–53.
8. M.A. Imam and R.G. Reddy: *Metall. Mater. Trans. B*, 2018, vol. 49B (6), pp. 3504–12.
9. M.A. Imam and R.G. Reddy: *Metall. Mater. Trans. B*, 2018, vol. 50B (1), pp. 981–90.
10. M.A. Imam and R.G. Reddy, *Applications of Process Engineering Principles in Materials Processing, Energy and Environmental Technologies*, Springer, 2017, pp. 457–64.
11. M.A. Imam and R.G. Reddy, *Mg Technology*, Springer, 2018, pp. 173–79.
12. M.A. Imam and R.G. Reddy: *High Temp. Mater. Process.*, 2019, vol. 38, pp. 411–24.
13. G.N. Makarenko, *In Boron and Refractory Borides*, ed. Vlado I. Matkovich, Springer, Berlin, 1977, pp. 310–30.
14. A. Mostafa and M. Medraj: *Materials*, 2017, vol. 10, p. 676.
15. R.W. Cahn: *Adv. Mater.*, 1991, vol. 3, pp. 628–29.
16. R.K. Bird, T.A. Wallace, and S.N. Sankaran: *J. Spacecr. Rockets*, 2004, vol. 41, pp. 213–20.
17. X. He, Y. Li, L. Wang, Y. Sun, and S. Zhang: *Thin Solid Films*, 2009, vol. 517, pp. 5120–29.
18. J. Matsushita and S. Komarneni: *Mater. Res. Bull.*, 2001, vol. 36, pp. 1083–89.
19. W.A. Tiller: *J. Electrochem. Soc.*, 1980, vol. 127, pp. 619–24.
20. W.A. Tiller: *J. Electrochem. Soc.*, 1980, vol. 127, pp. 625–32.
21. W.A. Tiller: *J. Electrochem. Soc.*, 1981, vol. 128, pp. 689–97.
22. Y. Wang and M. Trenary: *Chem. Mater.*, 1993, vol. 5, pp. 199–205.
23. Y. Wang, J. Fan, and M. Trenary: *Chem. Mater.*, 1993, vol. 5, pp. 192–98.
24. E.A. Irene and R. Ghez: *Appl. Surf. Sci.*, 1987, vol. 30, pp. 1–16.
25. I. Barin: *Thermochemical Data of Pure Substances*, VCH, Weinheim, 1989.
26. M.L. Whittaker, H.Y. Sohn, and R.A. Cutler: *J. Solid State Chem.*, 2013, vol. 207, pp. 163–69.
27. T.W. Jason, J.C. Daniel, E.H. Morgan, L.R. Andrea, C.I. David, K. Savas, M.J. Wojciech, and R. Faiz: *Semicond. Sci. Technol.*, 2016, vol. 31, p. 105007.
28. A. Bongiorno and A. Pasquarello: *Phys. Rev. Lett.*, 2002, vol. 88, p. 125901.
29. F.J. Norton: *Nature*, 1961, vol. 191, p. 701.
30. D.L. Poerschke, M.D. Novak, N.A. Jabbar, S. Krämer, and C.G. Levi: *J. Eur. Ceram. Soc.*, 2016, vol. 36, pp. 3697–3707.
31. D.V. Kolovertnov and I.B. Ban'kovskaya: *Glass Phys. Chem.*, 2015, vol. 41, pp. 324–28.
32. Y.L. Zhang, J.F. Huang, K.J. Zhu, L.Y. Cao, C.Y. Li, L. Zhou, B.Y. Zhang, W.H. Kong, and B. Zhang: *Appl. Surf. Sci.*, 2015, vol. 340, pp. 43–48.
33. G. Shao, X. Wu, Y. Kong, S. Cui, X. Shen, C. Jiao, and J. Jiao: *Surf. Coat. Technol.*, 2015, vol. 270, pp. 154–63.
34. A. Roine, *HSC Chemistry*, 2013, vol. 7.
35. M. Ramachandran, D. Mantha, C. Williams, and R.G. Reddy: *Metall. Mater. Trans. A*, 2011, vol. 42A, pp. 202–10.
36. C.M. Carney, T.A. Parthasarathy, and M.K. Cinibulk: *J. Am. Ceram. Soc.*, 2011, vol. 94, pp. 2600–07.
37. G.E. Murch: *Diffusion in Crystalline Solids*, Academic Press, New York, 2012.
38. W. Yang, W. Ao, J. Zhou, J. Liu, K. Cen, and Y. Wang: *J. Propul. Power*, 2013, vol. 29, pp. 1207–13.
39. C.H. Wen, T.M. Wu, and W.J. Wei: *J. Eur. Ceram. Soc.*, 2004, vol. 24, pp. 3235–43.

40. W. Kingery: *Introduction to Ceramics*, 2nd ed., Wiley, New York, 1976.
41. R.C. Jaeger: *Introduction to Microelectronic Fabrication: Modular Series on Solid State Devices*, Prentice Hall, Upper Saddle River, 2001, vol. 5.
42. D. Yu, C.D. Kong, J.K. Zhuo, S.Q. Li, and Q. Yao: *Sci. China Technol. Sci.*, 2015, vol. 58, pp. 2016–24.
43. J.W. Hinze, W.C. Tripp, and H.C. Graham, Systems Research Labs, Inc., Dayton, OH 1975.
44. W.C. Tripp and H.C. Graham: *J. Electrochem. Soc.*, 1971, vol. 118, pp. 1195–99.
45. J.B. Berkowitz-Mattuck: *J. Electrochem. Soc.*, 1966, vol. 113, pp. 908–14.

Publisher's Note Springer Nature remains neutral with regard to jurisdictional claims in published maps and institutional affiliations.